The influence of substitutional disorder on non-radiative transitions in Cr^{3+}-doped gallogermanate crystals

1997 J. Phys.: Condens. Matter 9 2815

(http://iopscience.iop.org/0953-8984/9/13/021)

J. Phys.: Condens. Matter **9** (1997) 2815–2829. Printed in the UK PII: S0953-8984(97)78985-9

The influence of substitutional disorder on non-radiative transitions in Cr^{3+}-doped gallogermanate crystals

Marek Grinberg†, Włodzimierz Jaskólski†, Peter I Macfarlane‡ and Keith Holliday‡

† Institute of Physics, N Copernicus University, Grudziadzka 5/7, 87-100 Toruñ, Poland
‡ Department of Physics and Applied Physics, University of Strathclyde, Glasgow G1 1XN, UK

Received 28 October 1996, in final form 13 January 1997

Abstract. The substitutionally disordered nature of gallogermanates creates a distribution of crystal-field strengths and symmetries for Cr^{3+} dopant ions. This causes the Huang–Rhys factor of the $^4T_2 \rightarrow {}^4A_2$ transition to vary from site to site, leading to a strongly broadened luminescence band. This luminescence is blue-shifted and strongly quenched with increasing temperature. Calculations show that this behaviour is due to large variations in the internal conversion rates for ions in different parts of the crystal-field distribution. It is shown that a confinement potential rather than a harmonic potential is required to account for the data.

1. Introduction

The optical properties of Cr^{3+} impurity ions have proved to be highly compatible with the parameters required for use as laser gain media, most recently in tunable and ultra-short-pulse all-solid-state lasers such as those based on Cr^{3+}-doped $LiSrAlF_6$. Due to the success of this and similar materials there is much interest in producing new gain media with improved or alternative properties and therefore in understanding the fundamental interactions that govern their behaviour. The Cr^{3+}-doped gallogermanate crystals were considered as candidates for broadly tunable laser action [1] as they are characterized by very broad luminescence bands and appeared to offer tuning ranges significantly shifted toward the infrared compared to most other hosts. Unfortunately, poor efficiencies and high thresholds make them unsuccessful as laser gain media. This paper is an investigation of non-radiative decay in the gallogermanates that is the underlying process responsible for the material's poor laser performance.

In previous papers that have investigated the broadening of both the R-line and broad-band transitions of Cr^{3+} ions in gallogermanate crystals [2–4] it has been established that low-symmetry distortions to the octahedron of oxygen ions that surround the optically active ion are of great importance. That the distortions are unequal for Cr^{3+} ions occupying ostensibly the same sites is due to the fact that some cation sites are occupied randomly by Ga^{3+} and Ge^{4+} ions (though long-range stoichiometry is maintained). Such a crystal is said to be substitutionally disordered. In the case of calcium gallogermanate ($Ca_3Ga_2Ge_4O_{14}$ or CGGO), which is the material chosen as a test case in this paper, the substitutionally disordered site of most importance is the crystallographically labelled 3f site [4]. Six such sites immediately surround the octahedron of oxygen ions that enclose the Cr^{3+} ion, thus giving rise to 2^6 possible configurations. All 64 configurations are statistically equally

0953-8984/97/132815+15$19.50

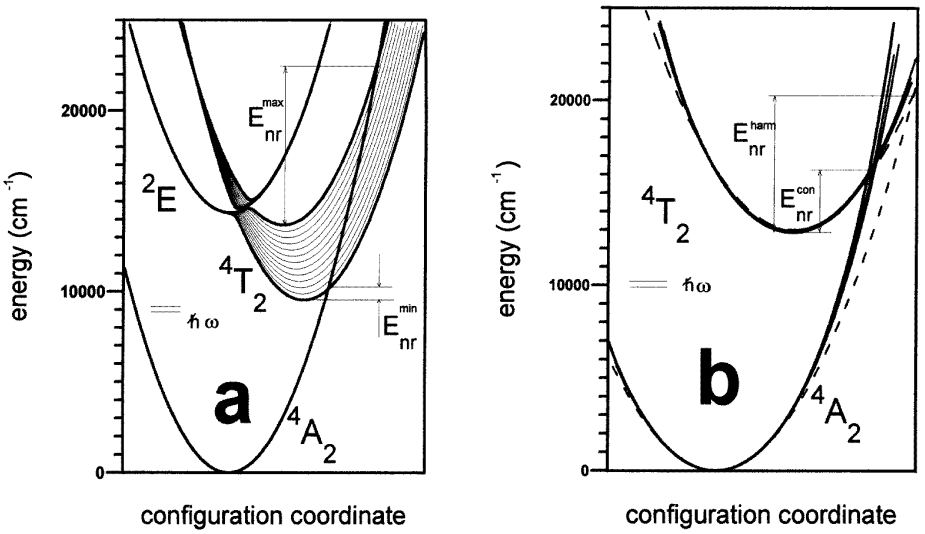

Figure 1. (a) A configuration coordinate diagram of the weak-field-site Cr^{3+} ion. The ground and the two excited electronic manifolds are presented in the diagram. Each curve corresponds to a different site from the weak-field-sites distribution. (b) A configuration coordinate diagram of the weak-field-site Cr^{3+} ion. In the diagram the ground, $^4A_2$, and the first excited, $^4T_2$, electronic manifolds are shown. Dashed curves correspond to the harmonic lattice potential; solid curves correspond to the confinement-type potentials (formula (13)), with $\alpha = 250, \alpha = 300$ and $\alpha = 350$. All of the potentials presented in (b) were fitted to get the same emission and absorption lineshape.

probable as the Ga^{3+} and Ge^{4+} ions are equally numerous in this centre, but charge-compensation considerations are likely to cause combinations that are dominated by a single ion to be less favoured.

One result of the variation of the local distortions of the Cr^{3+} environment is to create two sets of strongly broadened fluorescence spectra. One set of sites fluoresces via the $^2E \rightarrow {}^4A_2$, R-line transition and has been studied using fluorescence-line-narrowing spectroscopy [2, 3]. These sites are not influenced by the effects of non-radiative decay and are therefore not of interest here and will be ignored in what follows. Most of the sites decay via the $^4T_2 \rightarrow {}^4A_2$ transition which is characterized by much stronger electron–lattice coupling, resulting in broad-band emission. Of particular importance is the fact that the electron–lattice coupling constant and therefore the $^4T_2$-state relaxation energy changes from site to site resulting in broad distributions of these quantities throughout the crystal [2]. The dependence of the $^4T_2 \rightarrow {}^4A_2$ emission lineshape on the excitation energy was modelled, and it was found that a correlation exists between the relaxation energy of the $^4T_2$ state and the strength of the electron–lattice coupling, attributed to increasingly distorted Cr^{3+} sites being more strongly coupled to asymmetric phonon modes [2]. This model also showed that a contribution to the broadening is made by the variation in the actual crystal-field strength, essentially determined by the size of the octahedron of oxygen ions surrounding the Cr^{3+} ions, but that this is smaller than the influence of the site-to-site variation in the Huang–Rhys parameter. This applies to all members of the gallogermanate family regardless of the proximity of the substitutionally disordered site to the optically active ion [3].

As the large electron–lattice coupling shifts the excited electronic manifolds in

configuration space, non-radiative internal conversion processes become more likely to occur, and this decreases the quantum efficiency of the system. In this paper the kinetics of the non-radiative processes in the chromium sites in gallogermanates are analysed. It is shown that the low quantum efficiency of the chromium-doped gallogermanates is due to the domination of the non-radiative internal conversion process [5, 6], even at low temperatures. Such a situation is directly connected to the existence of the relationship between the energy of the $^4T_2$ state and the electron–lattice coupling energy. Additionally, the non-radiative processes are amplified by the effect of the confinement of the motion of the ions which has to be taken into account for large ionic displacements.

In figure 1(a), a schematic distribution of the weak-field Cr^{3+} sites in a typical gallogermanate, as determined previously [2], is presented. In the more distorted sites the $^4T_2$ electronic manifold is more strongly shifted in configuration coordinate space and relaxes to lower energy. For these sites the crossing of the $^4T_2$ and $^4A_2$ configurations occurs at a lower energy, E_{nr}, with respect to the minimum of the $^4T_2$ state than is the case for sites of higher symmetry. The maximum and minimum values of E_{nr} for the distribution are indicated on figure 1(a) and vary by about an order of magnitude, despite the fact that the minima of the potential wells vary by only about 40%. This is because of the duel influence of the reduction in energy of the potential well and the shift in configuration space. The probability of the non-radiative internal conversion process taking place thus increases rapidly as the oxygen octahedron is deformed. Additional lowering of the energy, E_{nr}, is related to the confinement of the ionic motion. In figure 1(b) the configuration coordinate diagram for a single Cr^{3+} site is presented. Lattice potentials have been approximated by a harmonic potential (dashed curves) and three confined potentials with different values of the confinement constant (solid curves), all of which correspond to a single ion having a certain electronic energy. Detailed descriptions of the potentials and approximations are given below, but it can be seen by inspection that E_{nr} is smaller for the confined potentials than for the harmonic wells, thus increasing the non-radiative conversion rate in the former case.

Using the ideas introduced above, this paper models the observed temperature dependence of the decay characteristics of Cr^{3+}-doped calcium gallogermanate, focusing on the fluorescence quenching and blue-shift of the $^4T_2 \rightarrow {}^4A_2$ emission peak with increasing temperature. The technique described is expected to be generally applicable and particularly useful for disordered materials.

2. Experimental details

The sample was a piece of laser-quality Cr^{3+}:CGGO and was mounted inside a Leybold variable-temperature cold-head refrigerator. The temperature could be controlled between 10 K and room temperature. Fluorescence was excited by the output of an argon-ion-laser-pumped dye laser with a linewidth of about 1 cm^{-1} operating at 600 nm. Emission was dispersed by a 0.5 m monochromator and detected by a cooled germanium detector. The laser was slowly chopped and the signal measured using a lock-in detector. The resulting spectra were corrected for instrumental response.

3. Theory

In order to explain how the temperature-dependent fluorescence spectra have been modelled it is first necessary to introduce a theoretical description of the environment of the Cr^{3+}

ion and the processes that determine whether a particular site will de-excite radiatively or otherwise.

3.1. Non-radiative transitions and the distribution of emitting sites

The quantum efficiency, η, of the system is a quantity which is proportional to the fraction of the sites contributing to the luminescence, and this varies with temperature. As the entire population of ions decays either radiatively or non-radiatively, η is given by the ratio of their respective probabilities, P_{rad} and P_{n-rad}:

$$\eta(T) = \frac{P_{rad}}{P_{rad} + P_{n-rad}(T)}. \tag{1}$$

Radiative transitions take place independently of temperature, and so temperature-dependent changes in the quantum efficiency must be related to non-radiative processes. In principle, P_{n-rad} takes into account all of the non-radiative decay processes but the analysis presented here assumes that by far the most important of these is internal conversion. A detailed description of the internal conversion processes in localized states in solids has been published previously [6, 7]. In this work an expression was derived for the probability, W^{nm}, of a transition from a particular vibronic state, n, of the excited electronic manifold, $^4T_2$, to that vibronic state, m, of the ground electronic manifold, $^4A_2$, that leaves the system with the same energy:

$$W^{nm} = \frac{2\pi}{\overline{h}\omega}|\langle\varphi_{^4T_2}|H'|\varphi_{^4A_2}\rangle|^2|F^{nm}_{^4T_2{}^4A_2}|^2\delta(E^n_{^4T_2} - E^m_{^4A_2}). \tag{2}$$

Here $\overline{h}\omega$ is the phonon energy, whilst $|\langle\varphi_{^4T_2}|H'|\varphi_{^4A_2}\rangle|$ and $|F^{nm}_{^4T_2{}^4A_2}|$ are, respectively, the electronic matrix element and the overlap integral of the vibronic wave functions. The Hamiltonian, H', mixes the electronic wave functions of the ground and excited states and thus allows the non-radiative internal conversion process to take place. For the specific case of interest here, that of the Cr^{3+} ion, H' is the spin–orbit interaction. This is non-vanishing between the $^4A_2$ state and the Γ_8 component of the $^4T_2$ states [8, 9]:

$$|\langle\varphi_{^4T_2}|H'|\varphi_{^4A_2}\rangle| = \sqrt{5/3}\zeta. \tag{3}$$

The quantity ζ is known as the spin–orbit parameter and is equal to a few hundred wavenumbers (cm^{-1}) with a weak dependence on the crystal host. Practically, it is preferable to work with the frequency factor, f:

$$f = \frac{2\pi}{\overline{h}\omega}|\langle\varphi_{^4T_2}|H'|\varphi_{^4A_2}\rangle|^2. \tag{4}$$

An accurate calculation of the spin–orbit parameter from first principles is not possible, but its value can be estimated from experimental evidence in this and related materials. The frequency factor can therefore also be estimated but, as the vibronic overlap integral can be accurately calculated, the frequency factor can be treated as a free parameter, limited within a certain physically realistic range. In this way, calculations using different models for the potential can be made and the frequency factor optimized to fit the data. If the frequency factor required is physically unrealistic then the model for the potential used in that calculation can be dismissed. It is also possible that the $^4T_2 \rightarrow {}^4A_2$ states are mixed by the lattice distortion of t_1 symmetry. Thus an additional non-radiative channel can depopulate the excited state. However, since the dominant modes in the electron–lattice coupling are the full symmetrical mode and two-dimensional e mode (which do not mix the T_2 and A_2 states), this additional channel, whilst possibly increasing the probability of internal conversion, is not the dominant non-radiative process.

The vibronic overlap integrals are given by

$$|F^{nm}_{^4T_2\,^4A_2}| = |\langle \chi^n_{^4T_2} | \chi^m_{^4A_2} \rangle|. \tag{5}$$

This expression effectively gives all of the information about the probabilities of internal conversion between the different vibronic states and implies the temperature dependence of the non-radiative transitions, as the frequency factor is a constant for a given pair of electronic manifolds. The temperature-dependent total probability of the non-radiative process is obtained by summation over all possible transitions:

$$P_{n-rad}(T) = \sum_{n=0}^{\infty} B_n(T) W^{nm} \tag{6}$$

where

$$B_n(T) = \exp\left(-\frac{E^n - E^0}{kT}\right) \Big/ \sum_m \exp\left(-\frac{E^m - E^0}{kT}\right) \tag{7}$$

is the Boltzmann occupation factor, E^n and E^0 are the energies of the respective vibronic states of the excited electronic manifold, and k is the Boltzmann constant.

Approaches where the overlap integrals have been calculated explicitly have been used by Struck and Fonger using the one-dimensional harmonic oscillator approximation [10, 11]. The two-dimensional case has been considered by Grinberg and Mandelis [7]. The nature of the electron–phonon coupling is complicated by the fact that the localized d electrons can interact with different lattice vibration modes (the ionic displacements which transform as the irreducible representation of the respective point group). For a system with O_h symmetry the electrons in the electronic state T_2 can interact with the fully symmetrical a_1 mode, the two-dimensional e mode, and the three-dimensional t_2 mode. Interaction with the a_1 mode causes only lattice relaxation, but on interaction with the e and t_2 modes a splitting also results. The latter are known as the Jahn–Teller $T * e$ and $T * t_2$ effects. Thus energy relaxation in the excited state can result from coupling to any of the three modes, whilst the configuration coordinate of the minimum of the excited state is shifted to a position defined by the n-dimensional vector $\boldsymbol{Q} = \{\boldsymbol{Q}_1, \boldsymbol{Q}_2, \ldots \boldsymbol{Q}_n\}$, where each $\boldsymbol{Q}_n$ corresponds to the component (or coordinate) of the respective normal mode. The energy relaxation is thus given by

$$S\bar{h}\omega = \frac{1}{2} \sum_i k_i \boldsymbol{Q}_i^2$$

where k_i is the elastic constant related to the ith shift. The static Jahn–Teller effect splits the electronic manifold into three and four equivalent paraboloids for $T*e$ and $T*t_2$ respectively, but as far as emission and excitation band-shapes are concerned they are indistinguishable from coupling to the symmetric mode, a_1. It is normally thought that coupling to the a_1 mode dominates in the case of octahedrally coordinated Cr^{3+} ions such as in garnets where the lattice relaxation energy is about 1500 cm^{-1}. For gallogermanates, $S\bar{h}\omega$ varies from site to site but is typically twice this value, and so it is expected that the Jahn–Teller coupling energy is significant, though it cannot be evaluated. However, it has been shown that the interaction with all of the phonon modes can be described by interaction with one effective mode [12] and that an effective coordinate given by

$$Q_{eff} = \sqrt{\sum_i k_i \boldsymbol{Q}_i^2}$$

can be defined. This is the approach taken here, and it has already been used, for instance, in figure 1 above. In fact, this is the only approach that is reasonable for such a complex modelling problem.

Since the probability of internal conversion, P_{n-rad}, depends on the energy and the position of the minimum of the excited electronic manifold, the quantum efficiency of the system also depends on these quantities according to equation (1). This means that sites from different parts of the distribution have different emission characteristics. Sites in the high- and low-energy wings of the distribution will decay almost exclusively radiatively and non-radiatively respectively. Those in between will show intermediate behaviour with a strong temperature dependence.

The effective 'emission distribution', Θ_{em}, is responsible for the emission lineshape and is related to the distribution of the excited sites, Θ_{exc}, thus:

$$\Theta_{em}(E_{exc}, E_{^4T_2}, T) = \Theta_{exc}(E_{exc}, E_{^4T_2})\eta(E_{^4T_2}, T). \tag{8}$$

Here E_{exc} and $E_{^4T_2}$ are the excitation energy and the energy of the minimum of the $^4T_2$ electronic manifold. Since the quantum efficiency, η, depends on temperature, changes in Θ_{em} are also expected, in particular a shift of the maximum of the effective distribution, Θ_{em}, to higher energy with increasing temperature. The prediction is therefore not only of emission quenching but also of a shift of the emission band toward higher energy. This effect has been observed experimentally for all of the gallogermanates investigated, as discussed below.

3.2. Calculations of the emission spectrum

The main parameter that will be used to compare experiment and theory for $^4T_2 \rightarrow {}^4A_2$ in what follows is the shift of the emission peak with temperature. This is the first moment of the spectrum, M^1:

$$E^{max} = M^1 = \int \mathrm{d}E\ I(E)E \tag{9}$$

where $I(E)$ is the normalized emission lineshape. The bandwidth is parametrized by the standard dispersion of the spectrum, D, which is related to the second moment of the spectrum, M^2, as follows:

$$D = \sqrt{M^2} = \sqrt{\int \mathrm{d}E\ I(E)[E - M^1]^2}. \tag{10}$$

The emission intensity has been reproduced as the convolution of the emission distribution with the overlap integral of the vibronic states in the ground and excited states, $P_e^{nm} = |F^{nm}_{^4T_2{}^4A_2}|^2$. The probability of the radiative transition depends on the same vibronic overlap integrals $|F^{nm}_{^4T_2{}^4A_2}|$ as for internal conversion, but different final states are selected by the appropriate Dirac delta functions; for internal conversion (formula (2)) an energy correspondence is required, whereas for radiative decay it is not. Finally, the Boltzmann occupation factor, B_n, defined by equation (7), is used to determine the vibronic state populations, and the final expression for the emission intensity becomes

$$I(E_{exc}, E) \propto \frac{E^3}{\tau} \sum_n \sum_m \int \mathrm{d}E_{^4T_2}\ \Theta_{em}(E_{exc}, E_{^4T_2}, T)B_n(T)P_e^{nm}\delta[E - (E^n_{^4T_2} - E^m_{^4A_2})]. \tag{11}$$

The absolute value of the radiative transition probability is considered to be proportional to the inverse of the low-temperature emission decay time, τ, at 10 μs [2].

3.3. The lattice vibration potential

Since the values of the vibronic overlap integrals are essential for calculations of the emission lineshape as well as for the non-radiative internal conversion rate, the shape of the potential of the lattice vibrations is an important feature to discuss. Two types of lattice vibration potential are discussed here. Both result in analytical solutions for the energy spectrum and for the vibronic wave functions. As described above (section 3.1), the physicality of the models can be determined after the frequency factor has been fitted to the data. The two models for the vibration potentials are the usual harmonic well and the confined potential, the latter representing the restrictions imposed by neighbouring ions and perhaps being more physically realistic for the large motions of the ions necessary for internal conversion to take place.

The harmonic potential, V, is represented by

$$V(Q) = \frac{1}{2}Q^2. \tag{12}$$

Here, the configuration coordinate, Q, is in units of $\sqrt{h/\mu\omega}$, where ω is the frequency of the phonon mode and m is the effective mass of the ions involved in the vibrations.

The confinement-type potential is given by [13, 14]

$$V(Q) = \frac{[\alpha(\alpha-1)]^{1/2}}{2}\tan^2\{Q[\alpha(\alpha-1)]^{-1/4}\} \tag{13}$$

which can be approximated by the harmonic potential of equation (12) for small Q. In equation (13), Q is related to the real ionic displacement, R, by

$$Q = R(\pi/A)[\alpha(\alpha-1)]^{1/4} \tag{14}$$

where A is the size of the confinement or, in other words, the absolute limit to the displacement of the ion. Thus,

$$[\alpha(\alpha-1)]^{1/2} = \frac{\omega\mu A^2}{h\pi^2}. \tag{15}$$

The vibronic wave functions for the potential given by equation (13) are

$$\chi_n(Q) = \sin^\alpha\{Q[\alpha(\alpha-1)]^{-1/4}\}C_n^{(\alpha)}\{\cos Q[\alpha(\alpha-1)]^{-1/4}\} \tag{16}$$

where the $C_n^{(\alpha)}$ are Gugenbauer polynomials. The vibronic wave functions in equation (16) correspond to the series of phonon energies, E^n, given by

$$E^n = [\alpha(\alpha-1)]^{-1/2}\left[\frac{n^2}{2} + \alpha\left(n+\frac{1}{2}\right)\right]. \tag{17}$$

The difference between the confined and harmonic potentials can be related to the value of a single parameter, α, or the physical parameter that corresponds to it: the confinement size, A. Full details of the confinement potential are described elsewhere [13, 14], but of importance here is the fact that the confinement potential yields a crossover of the energies of the ground and excited electronic manifolds for much lower energy than the corresponding harmonic potentials (see figure 1(b)). This results in much larger values of the overlap integrals describing the non-radiative processes for the confined potential.

Analysis of the experimental emission spectrum yields some of the parameters of the lattice potential. Regardless of which form of potential is used, the displacement of the ground and excited potentials in the configuration coordinate diagram, ΔQ, can be

determined from the energy separation of the maximum of the emission lineshape and the zero-phonon line, E_{rel}. The expressions for the two types of potential are

$$\Delta Q = \sqrt{\frac{2E_{rel}}{\hbar\omega}} \tag{18}$$

for the harmonic potential and

$$[\alpha(\alpha-1)]^{1/2}\tan^2\{\Delta Q[\alpha(\alpha-1)]^{-1/4}\} = 2\frac{E_{rel}}{\hbar\omega} \tag{19}$$

for the confined potential. The fits to the data that are carried out below require that α is of the order of a few hundred, and so expressions (18) and (19) yield similar values for ΔQ. In the same way, the confined potential does not differ very much in form from the harmonic potential for the first few tens of phonon excitations as can be seen for the curves in figure 1(b). From equation (17) it can be seen that for the confined potential the energy difference between successive vibronic energies increases as

$$1 + \frac{n+1/2}{\alpha^{3/2}(\alpha-1)^{1/2}}.$$

Thus, in this case, the parameter $\hbar\omega$ corresponds only to the energy of the zero-phonon excitation. In our calculations we have used $\hbar\omega = 250$ cm^{-1} for the harmonic approximation, whilst a slightly smaller value, $\hbar\omega = 240$ cm^{-1}, was necessary to fit the confined potential to the spectroscopic data.

3.4. The crystal-field distribution

The distribution of the crystal field is critical to the calculations described in this paper and therefore to a good understanding of the influence of substitutional disorder on the optical properties of impurity ions. It is necessary to perform calculations to determine the probabilities of radiative and non-radiative decay for all sites, the crystal-field parameters of which have been shown to vary over a large range due to the effect of substitutional disorder [2]. In order to model the behaviour it is initially assumed that a Gaussian distribution will describe the total variation in the energy of the $^4T_2$ manifold, $E_{^4T_2}$, relative to its peak, $E^0_{^4T_2}$, thus:

$$\Theta_{tot}(E_{^4T_2}) \propto \exp\left[-\frac{(E_{^4T_2} - E^0_{^4T_2})^2}{2\sigma^2}\right]. \tag{20}$$

For the fluorescing sites it has been shown [2] that $E_{^4T_2}$ is related to the electron–phonon coupling energy, E_{rel}, as follows:

$$E_{rel} = E^0_{rel} - K(E_{^4T_2} - E^0_{^4T_2}). \tag{21}$$

Here, K is a constant which describes the changes in the electron–phonon coupling for different sites within the distribution. When K is zero the electron–phonon coupling energy remains constant, and any change in the crystal field is considered to be purely in terms of its strength, causing no site-to-site shifts in the potential minima in configuration coordinate space. When K is non-zero there is a dependence of the electron–phonon coupling on $E_{^4T_2}$. This is explained physically in terms of distortions to the symmetry of the Cr^{3+} centre. More distorted sites couple more strongly to asymmetric phonon modes, thus shifting the potential minima in configuration coordinate space and reducing the energy. A value for K of 1 represents variation exclusively in the electron–phonon coupling. Values closer to 1 than 0 have been found for all gallogermanates [2, 3] and a typical distribution is shown

in figure 1(a). The value for CGGO was found to be 0.65 [2] and this value is used in all of the crystal-field distributions that are considered in this paper.

An additional complication is the fact that the crystal is excited by monochromatic laser light, so each site has its own excitation probability, P_{exc}, depending on its position in the distribution. Thus the distribution of sites actually excited, Θ_{exc}, is given by

$$\Theta_{exc}(E_{exc}, E_{^4T_2}) = \Theta_{tot}(E_{^4T_2})P_{exc}(E_{exc}E_{^4T_2}). \tag{22}$$

The probability of excitation, P_{exc}, is again given by the vibronic overlap integrals. For the harmonic vibronic potentials this leads to a Pekarian band-shape:

$$P_{exc}(E_{exc}, E_{^4T_2}) = \exp[-S(E_{^4T_2})]\frac{S^x(E_{^4T_2})}{x!} \tag{23}$$

where $S(E_{^4T_2}) = E_{rel}(E_{^4T_2})/\hbar\omega$ is the effective Huang–Rhys factor which describes the electron–lattice coupling for the individual site. For simplicity, the Pekarian has been used for all of the potentials considered. The quantity x is thought of as being the number of phonons released in de-exciting from the ground-electronic-state equilibrium position to the excited-electronic-state equilibrium position whilst in the excited state (in the harmonic approximation), but might generally be described by the quantity $(E_{exc} - E_{^4T_2})/\hbar\omega$.

Two distributions of the weak-field sites have been considered. The first has been taken directly from an analysis of the low-temperature emission spectra that took no account of non-radiative decay. The second distribution has been assumed to be much broader with the energies of the $^4T_2$ state extending to much lower values than for the former distribution. The narrower distribution of sites is considered as being the higher-energy part of the broader distribution, the justification being that the higher-energy sites are significantly less likely to decay non-radiatively than the low-energy sites. The values of the parameters that describe the distributions are listed in table 1.

Table 1. Parameters of the distribution of the crystal field. Broad distribution a was used for the harmonic potential whilst b was used for the confined potential.

	E^0_{max} (cm^{-1})	$E^0_{^4T_2}$ (cm^{-1})	K	σ (cm^{-1})
Previous distribution (narrow) [1]				
	3200	13 000	0.65	500
Broad distributions				
a	3850	12 000	0.65	750
b	3650	12 000	0.65	750

Since we considered the properties of the whole system at different temperatures, the shift of the energy of the $^4T_2$ state due to lattice expansion [15] should also be taken into account. The shift of the peak of the absorption band between 300 K and 77 K was found to be 0.5 cm^{-1} K^{-1}, and this figure has been linearly extrapolated for the range of experiments discussed here.

4. Results and discussion

To model the experimental data, four different lattice potentials have been used: the harmonic potential and three confined potentials with confinement constants of $\alpha = 250$, 300 and 350. The calculations have been performed for both the original crystal-field

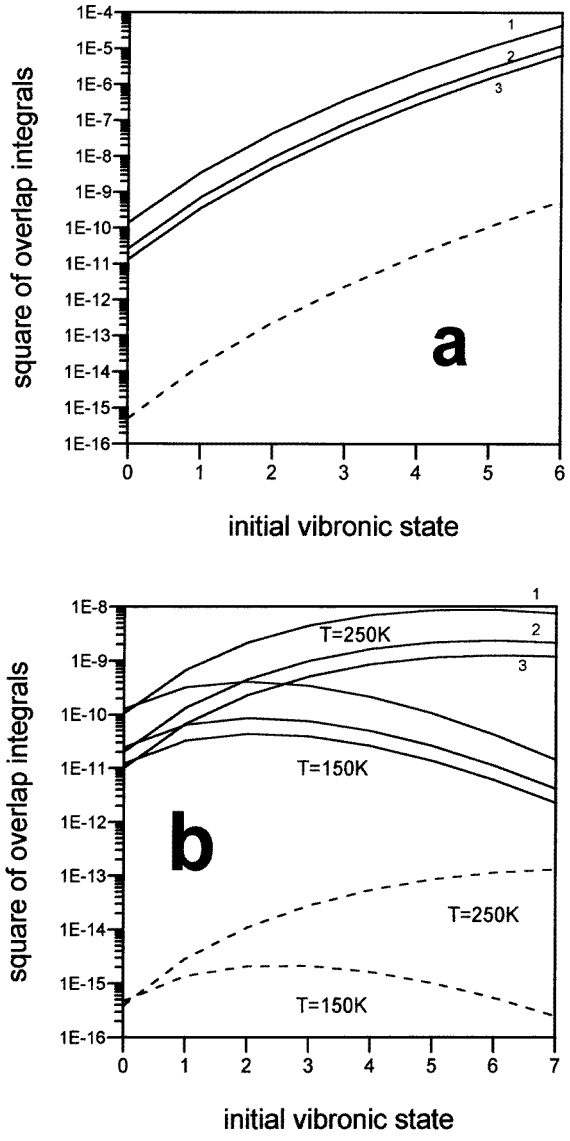

Figure 2. (a) The squares of the vibronic overlap integrals which control the non-radiative processes for various vibronic states of the excited electronic manifold for the potentials presented in figure 1(b)). The dashed curve corresponds to the harmonic potential; solid curves 1, 2 and 3 correspond to the confinement potentials with $\alpha = 250, 300$ and 350, respectively. (b) The squares of the vibronic overlap integrals multiplied by the Boltzmann factor for the temperatures 150 K and 250 K. The line types are as indicated for (a).

distribution, that describes the emission spectrum [2], and the extended distribution. The width of the extended distribution is treated as a free parameter, but slightly different widths are required to optimize the harmonic and confined potentials, labelled a and b respectively in table 1. All of the other crystal-field parameters are kept equal for both distributions.

The probability of the internal conversion process taking place is governed by the

dependence of the values of the vibronic overlap integrals on the energy of the vibronic quantum number of the initial state. In figure 2(a), for all four potentials considered, the calculated squares of the overlap integrals, $|F^{nm}_{^4T_2{}^4A_2}|^2$, are presented as functions of the initial vibronic state, n, for a value of m such that $E^n_{^4T_2} = E^m_{^4A_2}$. Figure 2(b) shows the same four curves after multiplication by the Boltzmann factor (equation (7)) for two different temperatures; they are thus proportional to the internal conversion probability according to equation (6). The constant of proportionality is the frequency factor. Even though the curves in figure 2(b) differ by orders of magnitude for the different potentials, the ratios between them remain almost the same, so picking the appropriate frequency factor for each will result in almost identical internal conversion probabilities. Under these circumstances, if it is possible to fit one potential to the data, then it will be possible to fit them all, though the frequency factor will vary between models by several orders of magnitude. As the frequency factor is determined by the spin–orbit matrix element, which is known reasonably well, it is easy to determine the feasibility of each potential model used.

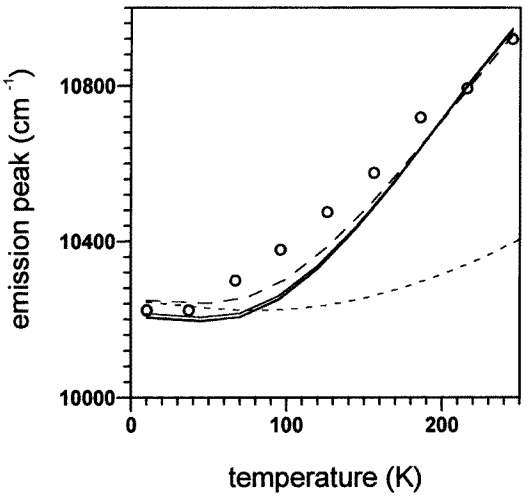

Figure 3. The temperature dependence of the maximum of the emission spectra of CGGO:Cr^{3+}. Circles correspond to the experimental data. Curves correspond to the computer-simulated dependencies: dashed curves were obtained for the harmonic approximation to the ionic vibration (small dashes correspond to the narrow distribution, large dashes correspond to the broad distribution a—see table 1); solid curves were obtained for the confinement-type potential, for broad crystal-field distribution b, for $\alpha = 250, \alpha = 300$ and $\alpha = 350$, with the other parameters as listed in table 1. As the solid curves are almost identical, they are not individually distinguished.

The experimental results for the shift of the peak of the band with wavelength are presented in figure 3 together with the results of several fits. The dashed curves correspond to results obtained for the harmonic potential using the narrow (small dashes) and broad (large dashes) distributions. Solid curves correspond to best fits for confined potentials.

When the narrow distribution of sites is used, small shifts of the emission peak with increasing temperature result. Only one curve is shown for the narrow distribution but, for both types of potential, the majority of sites decay radiatively. Even at higher temperatures the non-radiative transitions remain weak, so the effective emission distribution, Θ_{em} (equation (8)), does not change significantly, and the shift of the emission peak with

temperature is small. The narrow crystal-field distribution cannot reproduce the experimental dependence of the emission peak on temperature for any values of the frequency factor for any reasonable potentials. This distribution will therefore not be discussed any further.

Table 2. Parameters pertaining to the simulation of the dependence of the peak emission on temperature.

Curve	Potential type	Field distribution	Frequency factor (s^{-1})	Matrix element $\lvert\langle\varphi_{^4T_2}\rvert H'\rvert\varphi_{^4A_2}\rangle\rvert$ (cm^{-1})
Dashed	Harmonic	Narrow [1]	3×10^{14}	250
Large-dashed	Harmonic	Broad a	1×10^{18}	14 500
Solid	Confinement $\alpha = 350$ ($A = 6.6$ Å)	Broad b	7×10^{14}	380
	Confinement $\alpha = 300$ ($A = 6.1$ Å)	Broad b	2.4×10^{14}	220
	Confinement $\alpha = 250$ ($A = 5.6$ Å)	Broad b	5×10^{13}	100

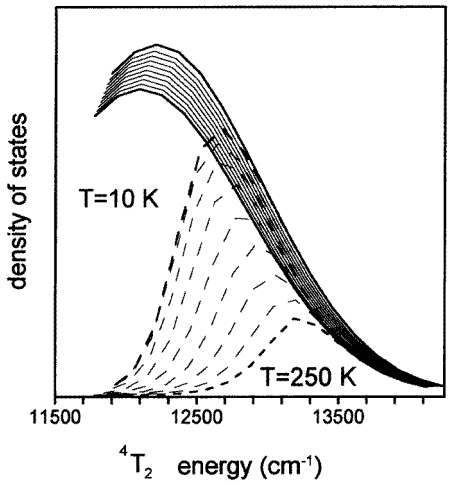

Figure 4. The weak-crystal-field site distribution. Dashed curves represent the distribution of the sites active in the emission $\Theta_{em}(E_{exc}, E_{^4T_2}, T)$; solid curves represent the distribution of the excited ions $\Theta_{exc}(E_{exc}, E_{^4T_2})$. Calculations have been performed for the confined potential with $\alpha = 300$, for the broad crystal-field distribution b (the other parameters are as listed in tables 1 and 2).

In the broader crystal-field distribution, only the high-field-tail sites have quantum efficiencies close to 1. For both types of potential the slopes obtained reproduce the temperature dependence of the emission peak well (figure 3). The large shift of the emission peak is the result of significant changes in the distribution of strongly radiative sites with temperature as described by equation (8). In figure 4, Θ_{em} is shown in comparison with Θ_{exc} for various temperatures. The solid lines represent the shift of Θ_{exc} as the lattice expands with temperature and the dashed lines show the subset of excited sites that decay

radiatively. In the lower-energy part of the distribution there is very little contribution to the emission since the quantum efficiency is close to zero at all temperatures. The sites from the higher-energy tail of the distribution always decay radiatively since, for stronger crystal-field and weaker electron–lattice coupling, the internal conversion processes are negligible. The sites that are responsible for the temperature shift of the emission peak are those that are intermediate in energy and have radiative and non-radiative probabilities of about the same order of magnitude, the dominant process depending on temperature. In the low-temperature limit, the effective emission distribution is similar to the distribution obtained when considering only radiative decay [2].

The curves in figure 4 correspond to the confined potential with $\alpha = 300$, requiring a frequency factor of 2.4×10^{14} s^{-1}. As discussed above, similar results were also obtained for each of the potentials considered by choosing a different value for the frequency factor, and these are summarized in table 2. As discussed in reference [6], the absolute value of the frequency factor is related to the physical phenomenon responsible for the non-radiative processes. For both of the interactions discussed in this paper, the frequency factor is not larger than 10^{13}–10^{15} s^{-1}. The value of 10^{18} s^{-1} obtained for the harmonic potential is therefore unrealistic, and the conclusion is that the confined potential is the better representation. All three of the confined potentials fall within the limits of credibility for the frequency factor required, and no firm conclusion is drawn as to the precise parameters that describe the potential. It is sufficient to say that the value of α is 300 ± 50 and the frequency factor is of the order of 10^{14}. These values may be used to calculate the confinement size according to equation (15), and the results are also shown in table 2 assuming the effective mass to be equal to that of six oxygen ions and taking the phonon energy to be 240 cm^{-1}. The confinement size is 6 Å, which is considered reasonable for a Cr^{3+}–ligand distance of 2 Å.

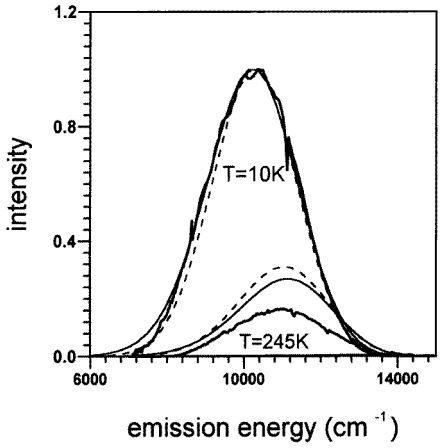

Figure 5. Simulated and experimental emission spectra for two different temperatures. Dashed lines correspond to the simulation using the harmonic potential, solid lines to that obtained using the confined potential with $\alpha = 300$. Solid bold lines represent the experimental spectra.

It is clear from figure 4 that many fewer sites contribute to the luminescence at higher temperatures. As a final check on the validity of the models put forward in this paper, the fluorescence band is constructed at two temperatures using the calculations outlined above, and these are presented in figure 5. The calculations predict a strong quenching

of the luminescence, but less than that observed experimentally. There are two possible explanations for this discrepancy. The first refers to the specific shape of the tails of the crystal-field distribution that has been assumed to be Gaussian. The quenching of the luminescence is very sensitive to the precise crystal-field distribution—in particular the wings of the distribution. Some of the crystal-field distribution parameters, such as K, have been transposed directly from calculations made on the low-temperature emission spectrum and may therefore be somewhat inaccurate, thus distorting the potential wells in configuration coordinate space. As discussed above, small changes in the position of a potential well lead to a large change in E_{nr} and thus to very large changes in the internal conversion rate. A second explanation is the existence of additional non-radiative processes that affect all of the sites in the same way. This additional process would cause further fluorescence quenching with increasing temperature without changing the position of the emission peak.

5. Conclusions

The radiative and non-radiative decay characteristics of chromium-doped calcium gallogermanate have been explained in terms of the influence of internal conversion on a broad crystal-field distribution. The temperature-dependent emission characteristics can only be described by using a confinement potential. This finding is physically realistic as very large vibrations, equivalent to tens of phonons, are necessitated by direct transfer from the excited state to the ground state, and this implies substantial ionic motion. It is physically realistic to expect that such large motion should be restricted by neighbouring ions.

It is hoped that this study will aid the development of gain media that may be designed to have similarly large tuning ranges without the thermal difficulties that gallogermanates experience. The broadening in gallogermanates occurs as a result of substitutional disorder causing variation in the magnitude of the Huang–Rhys parameter, but this is also the principal cause of the strong non-radiative decay. To find broadened transitions without non-radiative decay it may be necessary to search for materials in which the crystal-field strength varies but the Huang–Rhys factor remains at a relatively low value.

Acknowledgments

The authors are grateful to Professor Brian Henderson for the provision of equipment and for the instigation of this research programme, which has been supported by the EPSRC and MOD through research grants GR/F/54009 and GR/F/54105. Travel grants to support this collaborative project were kindly provided by a joint British Council and Komitet Badan Naukowych award.

References

[1] Kaminskii A A, Butashin A V, Demidovich A A, Koptev V G, Mill B V and Shkadarevich A P 1989 *Phys. Status Solidi* a **112** 197
[2] Grinberg M, Macfarlane P I, Henderson B and Holliday K 1995 *Phys. Rev.* B **52** 3917
[3] Macfarlane P I, Henderson B, Holliday K and Grinberg M 1996 *J. Phys.: Condens. Matter* **8** 3933
[4] Yamaga M, Macfarlane P I, Henderson B, Holliday K, Takeuchi H, Yosida T and Fukui H 1997 *J. Phys.: Condens. Matter* **9** 569
[5] Robinson G W and Frosch R P 1963 *J. Chem. Phys.* **37** 1962

Robinson G W and Frosch R P 1963 *J. Chem. Phys.* **38** 1187
[6] Grinberg M, Mandelis A and Fjeldsted K 1993 *Phys. Rev.* B **48** 5935
[7] Grinberg M and Mandelis A 1994 *Phys. Rev.* B **49** 12 496
[8] Sugano S, Tanabe Y and Kamimura H 1970 *Multiplets of Transition Metal Ions in Crystals* (New York: Academic)
[9] Runciman W A and Schroeder K A 1961 *Proc. R. Soc.* **265** 489
[10] Struck C W and Fonger W H 1975 *J. Lumin.* **10** 1
[11] Fonger W H and Struck C W 1975 *Phys. Rev.* B **11** 3251
[12] Grinberg M and Koepke Cz 1995 *J. Appl. Spectrosc.* **62** 97
Grinberg M and Koepke Cz 1996 *Proc 10th Feofilov Symp. on Spectroscopy of Crystals Activated with Rare-Earth and Transition-Metals Ions; Proc. SPIE* **2706** 121
[13] Grinberg M, Jaskolski W, Koepke Cz, Planelles J and Janowicz M 1994 *Phys. Rev.* B **50** 6504
[14] Grinberg M and Jaskolski W 1997 *Phys. Rev.* B at press
[15] Henderson B and Imbush G F 1989 *Optical Spectroscopy of Inorganic Solids* (Oxford: Clarendon)